ELSEVIER

Materials Science and Engineering A 480 (2008) 167–174

MATERIALS SCIENCE & ENGINEERING A

www.elsevier.com/locate/msea

Change in anisotropy of mechanical properties with β-phase stability in high Zr-containing Ti-based alloys

Mohamed Abdel-Hady *, Keita Hinoshita, Hiroki Fuwa, Yoshinori Murata, Masahiko Morinaga

Department of Materials Science and Engineering, Graduate School of Engineering, Nagoya University, Nagoya, Aichi 464-8603, Japan

Received 1 May 2007; received in revised form 28 June 2007; accepted 30 June 2007

Abstract

High Zr-containing β-type Ti-based alloys were designed using electronic parameters to investigate experimentally the effect of β-phase stability on their elastic and plastic properties. Texture structures formed by cold rolling or recrystallization were related closely to the β-phase stability and hence affected the mechanical properties. In tensile tests, as the β-phase stability decreased, non-linearity in the elastic zone was enhanced and the work hardening tended to be diminished. Also, it was found that the lower β-phase stability led to the weaker anisotropy of plastic properties, but to the stronger anisotropy of elastic properties.

Keywords: High Zr-containing Ti alloys; β-Phase stability; Mechanical properties; Texture; Elastic and plastic properties; Anisotropy

1. Introduction

Recently, considerable efforts have been devoted to exploring novel β-titanium alloys for biomedical applications because of their superior properties such as the superelasticity, shape memory, low Young's modulus, satisfactory biocompatibility, and better formability compared to the α and α + β titanium alloys [1–7]. The mechanical properties of the β-titanium alloys depend strongly on the presence of several phases (e.g., ω-phase and martensitic α″-phase) in them. The appearance of these phases could be controlled by either the optimized alloy design [6,7] or the materials processing [4].

Most of the β-Ti alloys possess good workability. It is possible to fabricate a cold-rolled sheet of the alloys by a reduction ratio higher than 90%. In this case strong textures are developed and the anisotropy in elastic and plastic properties is induced inevitably to the sheet, resulting in the modification of alloy properties such as the elastic modulus, elastic strain, Poisson's ratio, strength, ductility, toughness, magnetic permeability and the energy of magnetization [8]. In other words, the elastic and plastic properties of the alloy may be improved by using an orientation effect arising form the textures. It is, therefore, important to examine which kinds of textures can be developed in the β-Ti alloys under the given conditions of thermo-mechanical treatment and to investigate the texture effect on the elastic and plastic properties.

Recently an electronic parameter *e/a* (electron-per-atom ratio) and the $\overline{Bo}$–$\overline{Md}$ diagram have been used for the design of new β-type alloys (the so-called GUM metals) [6]. Here, $\overline{Bo}$ is the average bond order between atoms and $\overline{Md}$ is the average d-orbital energy level of the element in the alloy. This diagram has been explained elsewhere [7].

The β-type Ti-based alloys deform by either slip or twin mechanism [1,5]. The stress-induced martensitic transformation also takes place in some alloys upon applying external stress to them [4,5]. These phenomena emerge depending on the β-phase stability and hence will be controlled by alloying. Also, it is known that the slip/twin boundary is close to the β/β + ω + (α″) boundary [7]. At this boundary, the elastic anisotropy factor, $A = C_{44}/C'$, is rather high since the value of the elastic shear modulus, $C' = (C_{11} - C_{12})/2$, is diminishing as the alloy approaches this boundary [9,10]. Also, it has been reported that the $(C_{11} - C_{12})/2$ value approaches zero when the *e/a* value is about 4.24 [9]. This is a reason why, in this work the *e/a* value was kept at 4.24 in all the designed alloys.

* Corresponding author. Tel.: +81 8051021411; fax: +81 527893233.
E-mail address: geprell@yahoo.com (M. Abdel-Hady).

0921-5093/$ – see front matter © 2007 Elsevier B.V. All rights reserved.
doi:10.1016/j.msea.2007.06.083

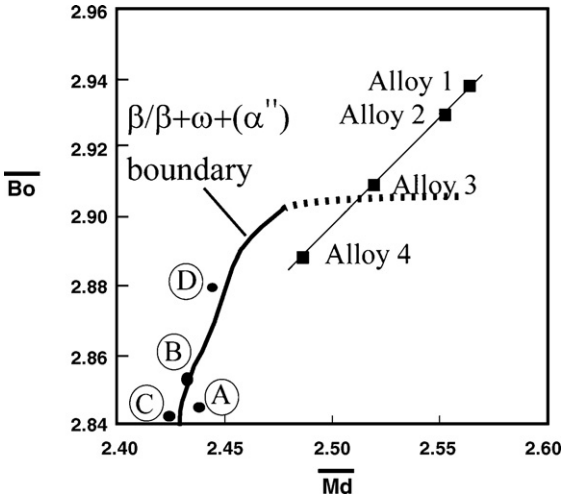

Fig. 1. Extended $\overline{Bo}$–$\overline{Md}$ diagram showing the $\beta/\beta+\omega$ $(+\alpha'')$ phase boundary and the location of the designed alloys, 1–4. Also, the alloys A, B, C, and D are 35 mass% Nb–4 mass% Sn, Ti–24Nb–3Al, Ti–35 mass% Nb–7.9 mass% Sn, and Ti–22Nb–6Ta, respectively.

This work is an extension of our previous study [7], and the β-phase stability effect was investigated on the anisotropy of mechanical properties and on the texture developed by cold rolling of four high Zr-containing alloys. Their alloy locations are indicated in the $\overline{Bo}$–$\overline{Md}$ diagram shown in Fig. 1. These β-type Ti alloys appear to be located in the positions across the $\beta/\beta+\omega+(\alpha'')$ phase boundary.

2. Experimental procedure

As explained above, four high Zr-containing alloys were designed and the chemical compositions are listed in Table 1. In this paper, all the compositions are given in atomic percent units unless otherwise noted. These alloys were prepared by the arc-melting of an appropriate mixture of pure metals (purity: 99.99%) under a high purity argon gas atmosphere. The button-shaped specimens with average 7.5 mm in thickness were cut and homoginized at 1273 K for 7.2 ks, and then cold rolled to the plate with 4.5 mm thick, followed by the solution treatment at 1223 K for 1.8 ks. This primary solution-treated specimen is called STBCR specimen. Subsequently, the specimen was cold rolled by 30 or 60 or 90% reduction in thickness. The cold-rolled specimen is called CR specimen hereafter. The 90% CR specimen was then solution treated at 1223 K for 1.8 ks. This finally solution-treated specimen is called ST specimen hereafter.

The phases existing in the specimen were identified by the conventional X-ray diffraction (XRD) using a Ni-filtered Cu Kα radiation. Electron back scattered diffraction (EBSD) analysis was also made using a HITACHI S-3000H scanning electron microscope (SEM) equipped with a OXFORD INCA Crystal EBSD detector, operated at an acceleration voltage of 20 kV and a tilt angle of 71°. The microstructural characterization was performed using the optical microscope (OM) and the scanning electron microscope (SEM). The micro-Vickers hardness was measured at a load of 20 N. The tensile test was carried out with both the ST and 90% CR specimens where the tensile axis was set to be parallel to either the rolling direction (RD) or the direction of 45° inclined to RD (45°). A cross-head strain rate used was fixed at $1.6 \times 10^{-4}\ s^{-1}$. Also, tensile loading and unloading tests were repeated at the stage of 1 and 2% strain, then loading was continued until fracture. The tensile strain was detected by both a standard strain gauge and a CCD camera.

Table 1
Chemical compositions (at.%) of the designed alloys

	V	Cr	Mo	Nb	Ta	Zr
Alloy 1	4		2	9	7	30
Alloy 2			3	15	3	25
Alloy 3		1		8	14	15
Alloy 4				4	20	5

3. Results and discussion

3.1. Change in β-phase stability with four alloys

The β-phase stability increases with increasing content of the β-stabilizing elements. Shown in Fig. 2 are the X-ray diffraction patterns taken from the four designed alloys in the STBCR condition, the 60% cold rolled (60CR) condition and the ST condition. In all the conditions, a single β-phase was predominant in the alloys 1, 2, and 3. Only in the alloy 4, the martensite α″-phase coexisted with the β-phase, as shown in Fig. 2(d). Therefore, the $\beta/\beta+\alpha''$ boundary shown in Fig. 1 is located between the alloys 3 and 4 as indicated by a dotted curve. So, the alloy 3 is the least stable single β-phase alloy which is defined as the alloy containing a least amount of the β-stabilizing elements to get a β-single phase. According to the $\overline{Bo}$–$\overline{Md}$ diagram shown in Fig. 1, the alloy closer to the $\beta/\beta+\alpha''$ boundary has the lower β-phase stability, so the β-phase stability in these alloys decreased in the order, alloy 1 > alloy 2 > alloy 3 > alloy 4. The stability was highest in the alloy 1 and lowest in alloy 4.

3.2. Textures developed by cold rolling

It is known that the cold rolling texture is formed in conventional β-type Ti alloys. As a result, the measured X-ray peak intensity ratio of the cold-rolled specimen, I_{Rcr}, defined as $I_{Rcr} = I_{\{200\}\beta}/I_{\{110\}\beta}$, changed with cold rolling. Here, $I_{\{200\}\beta}$ and $I_{\{110\}\beta}$ are the X-ray peak intensities of the $\{200\}_\beta$ and $\{110\}_\beta$ reflections, respectively. The I_{Rcr} increased with the reduction ratio of cold rolling. As is evident from Fig. 2 and Table 2, when the alloys were cold rolled by 60%, I_{Rcr} tended to increase with increasing β-phase stability. In other words, a cold rolling texture was developed in the way that the $\{200\}$ planes aligned parallel to the rolling plane preferentially. This texture was formed more readily in the order, alloy 1 > alloy 2 > alloy 3 > alloy 4, in agreement with the order of the β-phase stability.

Fig. 3a–c shows $\{200\}$, $\{110\}$ and $\{112\}$ pole figures obtained from a 90% cold rolled (CR) specimen of the alloy 2. The center of the pole figures corresponds to the direction normal to the specimen surface (ND). The right and the top of the pole figures corresponding to the rolling direction (RD) and the

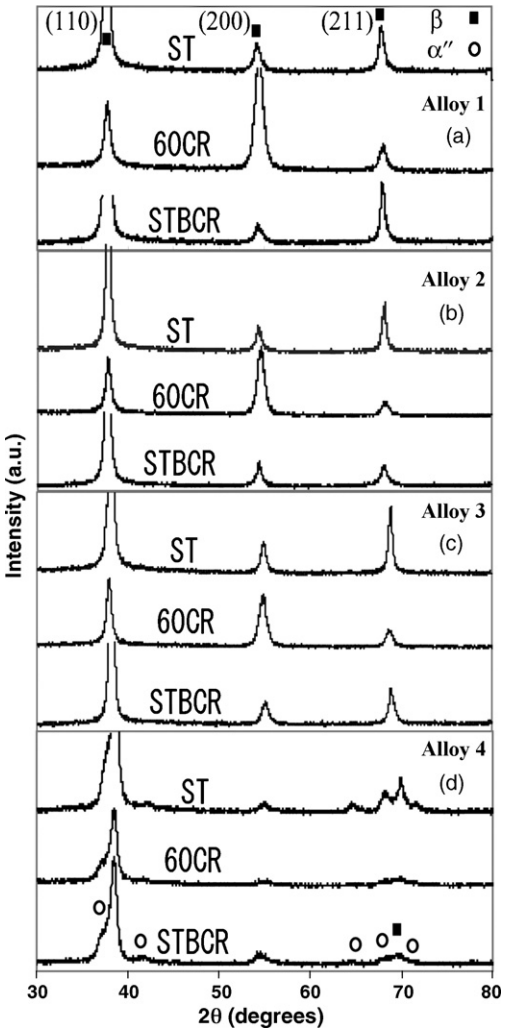

Fig. 2. XRD profiles after solution treatment before final cold rolling, STBCR, after 60% cold rolling, 60CR, and after 90% cold rolling followed by solution treatment at 1223 K, ST, of the alloys 1 (a), 2 (b), 3 (c) and 4 (d).

Table 2
X-ray peak intensity ratios in the ST and 60% cold rolling (60CR) conditions of alloys 1–4

	Alloy			
	1	2	3	4
60CR, $I_{Rcr} = I_{\{200\}\beta}/I_{\{110\}\beta}$	1.7	1.2	0.8	0.1
ST, $I_{Rst(1)} = I_{\{110\}\beta}/I_{\{200\}\beta}$	6	8.6	8.5	33
ST, $I_{Rst(2)} = I_{\{211\}\beta}/I_{\{200\}\beta}$	1.6	2	2.2	3.6

transverse direction (TD), respectively. It is realized from these pole figures that typically $\{1\,0\,0\}\langle 1\,1\,0\rangle$ rolling texture with a strength of 97.5 times larger compared to the random orientation is well developed in the 90% cold rolled (CR) specimen of the alloy 2 as shown in the $\{1\,0\,0\}\langle 1\,1\,0\rangle$ texture stereoprojection [11] in Fig. 3d. It is important to mention here that the alloy 2 with the relatively high β-phase stability shows the $\{1\,0\,0\}\langle 1\,1\,0\rangle$ texture after 90% CR more remarkably, as compared to the lower β-phase stability alloy undergone by the same or even severer cold rolling [3,4,12].

It has been reported that the $\{1\,0\,0\}\langle 1\,1\,0\rangle$ texture is a main rolling texture formed in the β-type Ti alloys [1,3,4,11,13]. Beside this texture, the $\{2\,1\,1\}\langle 1\,1\,0\rangle$ texture forms in a Ti–35 mass% Nb–4 mass% Sn alloy [4,11] (location A in Fig. 1) or the $\{1\,1\,1\}\langle 1\,1\,2\rangle$ texture forms in a Ti–24Nb–3Al alloy [11] (location B in Fig. 1). With a little increase in the β-phase stability, the $\{1\,0\,0\}\langle 1\,1\,0\rangle$ texture becomes dominant as observed in a Ti–35 mass% Nb–7.9 mass% Sn alloy [12] (location C in Fig. 1). As explained in Ref. [7], both Al and Sn work as the β-stabilizing elements in these β-phase alloys. In the much higher β-phase stability alloys such as Ti–22Nb–6Ta alloy (location D in Fig. 1), only the $\{1\,0\,0\}\langle 1\,1\,0\rangle$ texture is developed after 99% cold rolling [3]. This was consistent with the present results that the I_{Rcr} increases monotonously with the β-phase stability.

As crystal deforms by slip, it undergoes crystal rotations. Such rotations lead to the development of preferred orientations in polycrystalline alloys [14]. The main reason why the $\{1\,0\,0\}\langle 1\,1\,0\rangle$ texture develops by cold rolling in conventional bcc alloys may be attributable to the glide of dislocations along $\langle 1\,1\,1\rangle$ on $\{0\,1\,1\}$, $\{1\,1\,2\}$ or $\{1\,2\,3\}$ [15] and the crystal rotations in them. It is well known that C' represents the resistance for the $\{0\,1\,1\}\langle 0\,1\,1\rangle$ shear and C_{44} represents the resistance for the $\{0\,0\,1\}\langle 0\,0\,1\rangle$ shear [16] and both of them decreases with decreasing β-phase stability [3,10]. The *e*/*a* value is kept at 4.24 in the present alloys and C' decreases with decreasing β-phase stability as discussed earlier, so the elastic softening will be enhanced in the order; alloy1 < alloy 2 < alloy 3 < alloy 4. This is a reason why the alloys locating at the $\beta/\beta+\alpha''$ boundary showed a very low shear modulus along both $\langle 0\,1\,1\rangle$ on $\{0\,1\,1\}$ and along $\langle 1\,1\,1\rangle$ on $\{0\,1\,1\}$, $\{1\,1\,2\}$ or $\{1\,2\,3\}$ as reported in Ref. [6]. So it is expected that as the β-phase stability decreases, secondary slipping systems such as $\{0\,1\,1\}\langle 0\,1\,1\rangle$ may be activated by deformation beside the main slipping system, i.e., $\langle 1\,1\,1\rangle$ on $\{0\,1\,1\}$, $\{1\,1\,2\}$ or $\{1\,2\,3\}$. As a result, a portion of the applied stress is consumed in slipping in such secondary slipping sys-

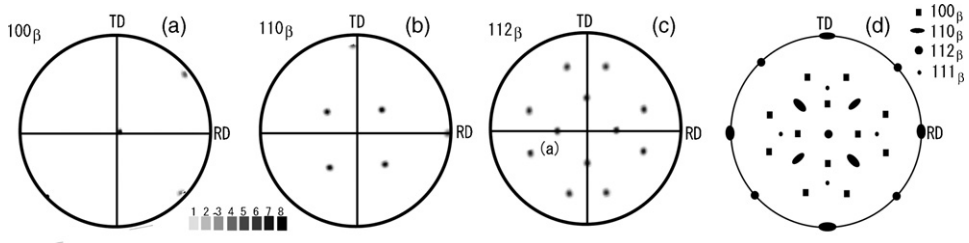

Fig. 3. EBSD pole figures of alloy 2 specimen after 90% cold rolling using 200_β (a), 110_β (b) and 112_β (c) and the stereoprojection of the $\{1\,0\,0\}_\beta\langle 1\,1\,0\rangle_\beta$-type texture (d).

tems, which will make some disturbances in forming the main $\{1\,0\,0\}\langle 1\,1\,0\rangle$ rolling texture. This can be a reason why the $\{1\,0\,0\}\langle 1\,1\,0\rangle$ rolling texture was dominant in the high β-phase stability alloys. This was also seen in the steel in which the addition of a ferrite (bcc) stabilizer, Si, is enhanced to form the rolling texture [14].

3.3. Textures developed by recrystallization

In the other case, the recrystallization texture was developed in the ST specimen that was solution treated after cold rolling. In Fig. 2 and Table 2, the X-ray peak intensity and the intensity ratios are shown of the ST specimen solution treated after 90% cold rolling. Here, $I_{Rst(1)}$ and $I_{Rst(2)}$ were defined as $I_{Rst(1)} = I_{\{1\,1\,0\}\beta}/I_{\{2\,0\,0\}\beta}$ and $I_{Rst(2)} = I_{\{2\,1\,1\}\beta}/I_{\{2\,0\,0\}\beta}$, respectively. Both of them decreased monotonously with increasing β-phase stability. Namely, in the recrystallization texture the high atomic density planes, i.e., $\{1\,1\,0\}$ and $\{2\,1\,1\}$, aligned parallel to the rolling plane preferentially. This trend further increased with decreasing β-phase stability, as shown in Table 2.

In Fig. 4, the Euler space plots are shown of the ST specimen of the alloys 2–4 which were subjected to solution treatment at 1223 K for 1.8 ks after 90% cold rolling. The Euler space density maps showed that the recrystallization texture was well developed in the alloy 4, followed by the alloy 3 and then the alloy 2. Thus, the tendency of forming the recrystallization texture in the alloys changed in the order, alloy 4 > alloy 3 > alloy 2, which was the opposite order of the rolling texture formed by cold rolling.

In the solution treatment after cold rolling, it has been reported that $\{1\,1\,2\}\langle 1\,1\,0\rangle$ recrystallization texture is mainly developed in the low β-phase stability alloys such as Ti–24Nb–3Al alloy [1,11] and Ti–35 mass% Nb–4 mass% Sn alloy [4,12]. Beside this $\{1\,1\,2\}\langle 1\,1\,0\rangle$ recrystallization texture, the $\{1\,1\,0\}\langle 2\,1\,1\rangle$ texture is developed in a little higher β-phase stability alloy, Ti–35 mass% Nb–7.9 mass% Sn [12]. However, only the $\{1\,1\,2\}\langle 1\,1\,0\rangle$ recrystallization texture appears in the Ti–22Nb–6Ta alloy [3]. It is important to note here that the $\{2\,1\,1\}\langle 1\,1\,0\rangle$ recrystallization texture is well developed in the alloy only after severe cold rolling (i.e., 95 and 99%) [3,13] and it tends to diminish with decreasing reduction ratio of cold rolling [3]. Also, recrystallization textures could be controlled by the temperature and time for the heat treatment [13].

Recrystallization is the replacement of deformed grains by the recrystallized grains [8]. The grains with certain crystallographic orientations will be nucleated and grown in the course of annealing [17]. The growth rate of the grains is also 'oriented', because some grains with certain crystallographic orientation will grow faster than others [14]. Otherwise, 'oriented' nucleation may control the final texture structure. As discussed earlier, both the elastic softening and the elastic anisotropy becomes more remarkable with the decrease in the β-phase stability. So, it was likely that the oriented nucleation and/or oriented growth was enhanced with decreasing β-phase stability, leading to the increase in the strength of the recrystallization texture.

From these discussions and the data given in Table 2, it was concluded that the tendency of forming the $\{1\,0\,0\}\langle 1\,1\,0\rangle$ texture by cold rolling increased with increasing β-phase stability, whereas the tendency of forming the recrystallization texture increased with decreasing β-phase stability. Thus, the β-phase stability was operating in the completely reverse way between the rolling and the recrystallization textures.

3.4. Microstructure change after cold rolling with β-phase stability

The microstructures are shown in Fig. 5 of the 90% cold rolled (90CR) alloys in the RD and the TD cross-sections. The stream-like deformation bands were observed clearly along the RD and TD directions in both the RD and TD cross-sections. As the β-phase stability decreased, the deformation bands seemed to become finer. Also the density of the deformation bands seemed to be higher in the TD cross-section shown in Fig. 5a than in the RD cross-section shown in Fig. 5b.

The microstructure in an enlarged magnification is shown in Fig. 6 for the 90CR alloys. In the alloy 4, fine shear bands with an angle 42° inclined to the main deformation band were observed in the RD cross-section. However, no such shear bands were observed in the TD cross-section. Also in the alloy 3, the secondary finer deformation bands with the angles of 23° and 37° inclined to the main deformation bands were observed in the RD and TD cross-sections, respectively. Neither the shear bands nor the secondary deformation bands were observed in the alloy 2 in both the RD and TD cross-sections. These results can be interpreted as due to the presence of the texturing systems other than $\{1\,0\,0\}\langle 1\,1\,0\rangle$ developed by the cold rolling and the plastic deformation among these three alloys depending on the β-phase stability. Also, the similarity in the TD and RD microstructure in the alloy 2 is attributable to the well developed $\{1\,0\,0\}\langle 1\,1\,0\rangle$ rolling texture in which both the RD and the TD are parallel to $\langle 1\,1\,0\rangle$ [3].

The microstructures are shown in Fig. 7 of the ST alloys solution treated at 1223 K for 1.8 ks after 90% cold rolling. Shear

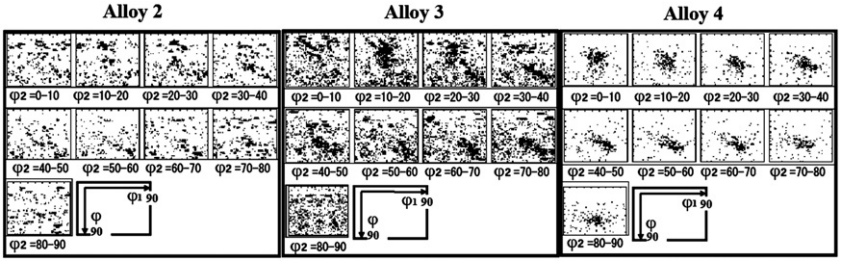

Fig. 4. φ_2 sections of the EBSD Euler space plot of alloys 2–4 specimens solution treated at 1223 K for 1.8 ks after 90% cold rolling.

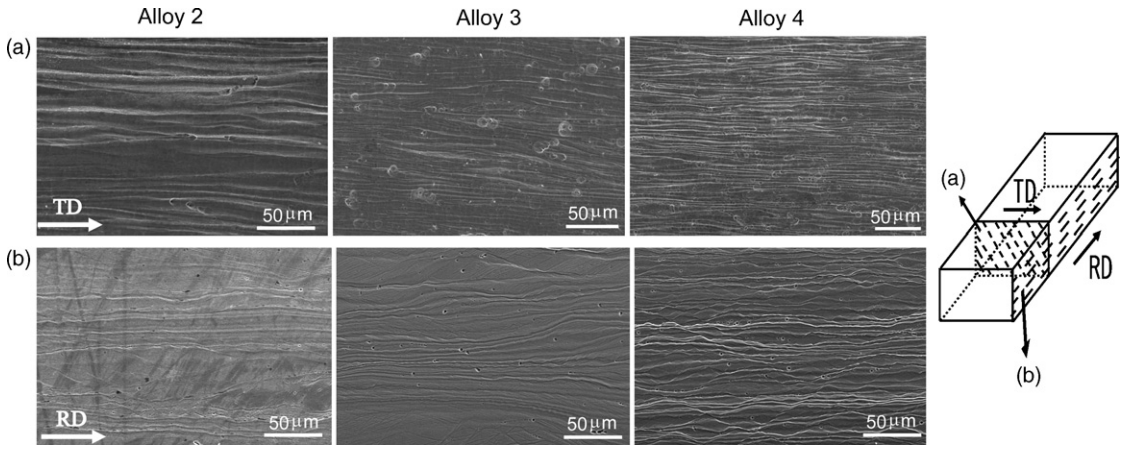

Fig. 5. SEM micrographs of alloys 2–4 after 90% cold rolling in the transverse, TD, cross-section (a), and in the rolling (RD), cross-section (b).

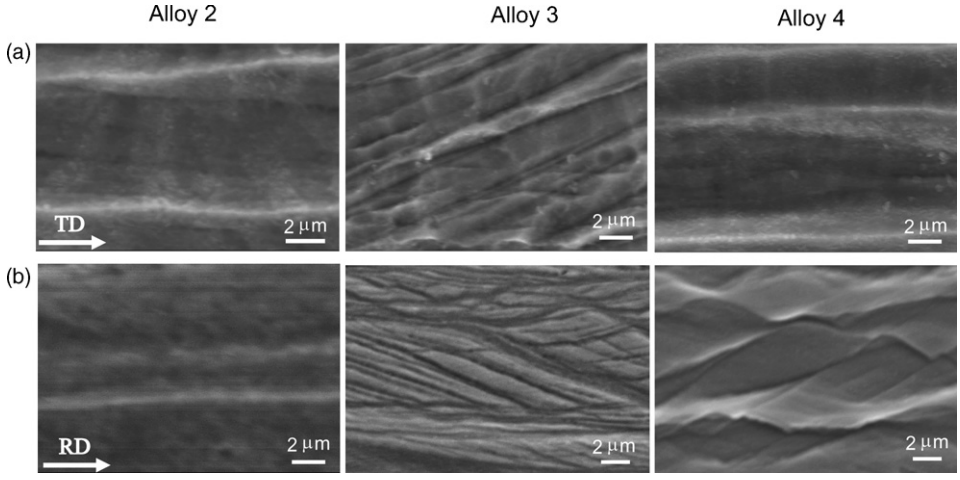

Fig. 6. SEM micrographs of alloys 2–4 shown in the enlarged scale of Fig. 5(a) and (b).

bands supposedly provide the majority of nucleation sites during recrystallization in the severely cold-rolled alloys. In particular, the triple joints between shear bands sites will work as nucleation sites [18]. So, the number of the nucleation sites was supposed to increase with decreasing β-phase stability, judging form the former deformation microstructures shown in Figs. 5 and 6. As a result, the grain size in the ST condition seems to decrease as the β-phase stability decreases. As is evident from the slightly defocused micrographs shown in Fig. 7a some deformation bands still existed in the TD cross-section, although the recrystal-

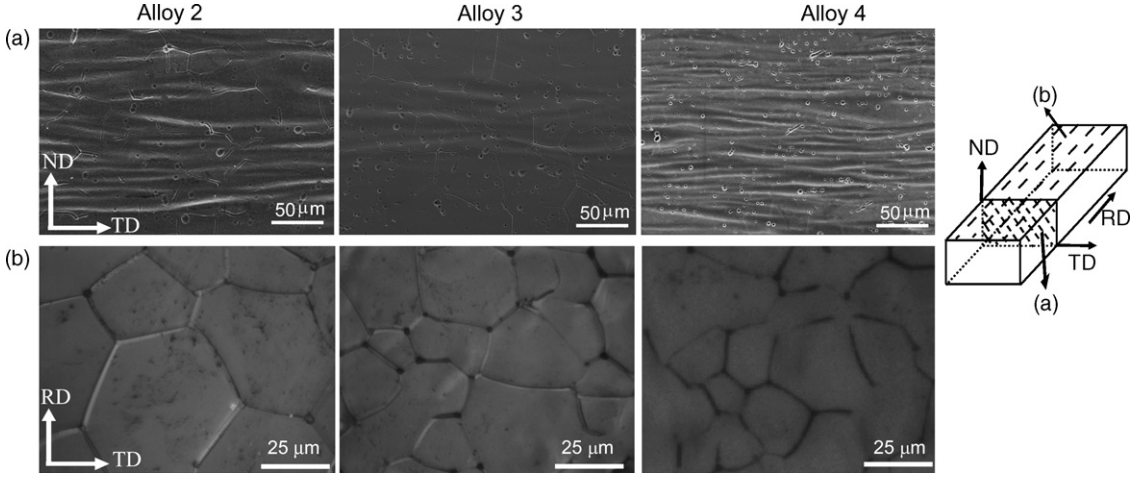

Fig. 7. Micrographs of alloys 2–4 after solution treatment at 1223 K for 1.8 ks after 90% cold rolling in the transverse, TD, cross-section, defocused SEM micrographs to show the deformation bands (a), and in the rolling plane, OM (b).

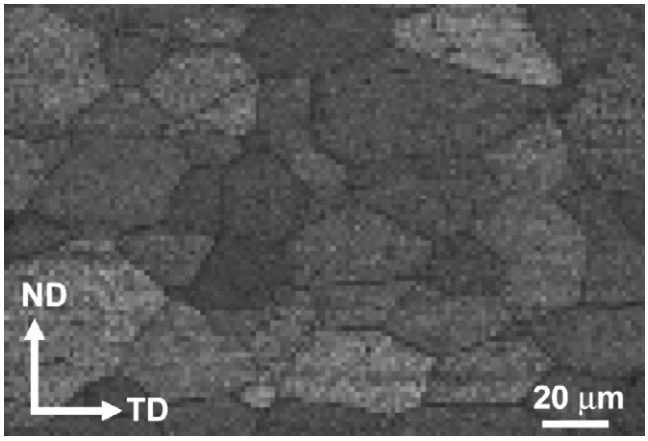

Fig. 8. EBSD image quality map (IQM) of solution-treated alloy 2 specimen at 1223 K for 1.8 ks after 90% cold rolling in the transverse cross-section, where equiaxed recrystallized grains are seen.

lization process seemed to be completed in the rolling plane shown in Fig. 7b. However, as shown in Fig. 8, the equiaxed grains were observed in the TD cross-section of the alloy 2 in the ST condition in the EBSD image quality map (IQM). Similar deformation bands were observed in a Ti–45Nb alloy in the recrystallized condition after severe cold working [19]. The reason why these deformation bands still remained after the recrystallization treatment is not clear at the moment.

3.5. Change in plastic properties with β-phase stability

The effect of cold rolling on the micro-Vickers hardness of the alloys is shown in Fig. 9. The hardness tended to increase as the β-phase stability increased. As shown in Table 3 this trend was also seen in the ultimate tensile strength (UTS), and in the elastic limit strength (ELS) defined as a maximum strength in the stress–strain relation without hysteresis. For example, the alloy 2 in the ST condition showed the larger UTS than the others. The alloy 4 where the α″-phase coexisted with the β-phase, had the least UTS and ELS values due to its poor β-phase stability and a

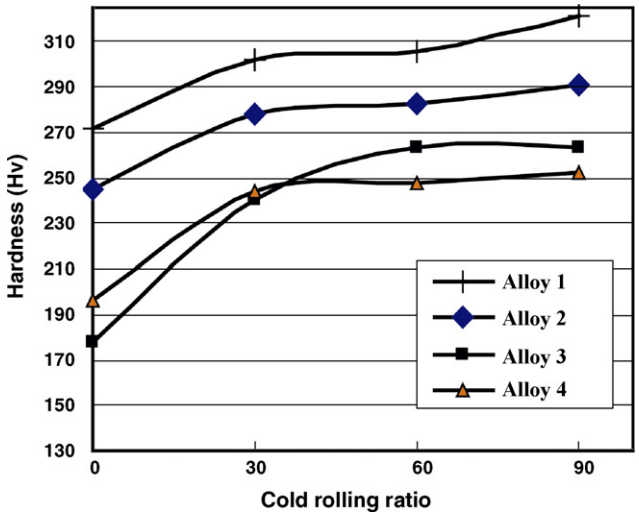

Fig. 9. Cold rolling effect on the micro-Vickers hardness of alloys 1–4.

Table 3
Mechanical properties of alloys 2–4 in the ST and 90CR conditions along the rolling direction, RD, and 45° to RD

Alloy no.	90CR		ST	
	RD	45° to RD	RD	45° to RD
UTS (MPa)				
Alloy 2	1094	974	742	726
Alloy 3	959	947	672	696
Alloy 4	936		583	
Elastic limit strength (MPa)				
Alloy 2	1032	901	698	699
Alloy 3	890	882	582	637
Alloy 4	865		556	
Resilience (YTPa)				
Alloy 2	525	640	270	260
Alloy 3	640	650	360	460
Alloy 4	870			

portion of the applied stress was consumed in the α″-martensitic transformation in it.

The present explanation was further confirmed in the results of the stress–strain curves obtained by the loading and unloading tensile test shown in Fig. 10b. Also, as shown in Fig. 10a, the alloy 4 in the ST condition exhibited two-steps yielding during the tensile test (as referred by the arrows in Fig. 10a) which is a well-known phenomenon for the stress-induced martensitic transformation. In this alloy 4, pseudoelasticity behavior was observed and there was a considerable unrecovered strain

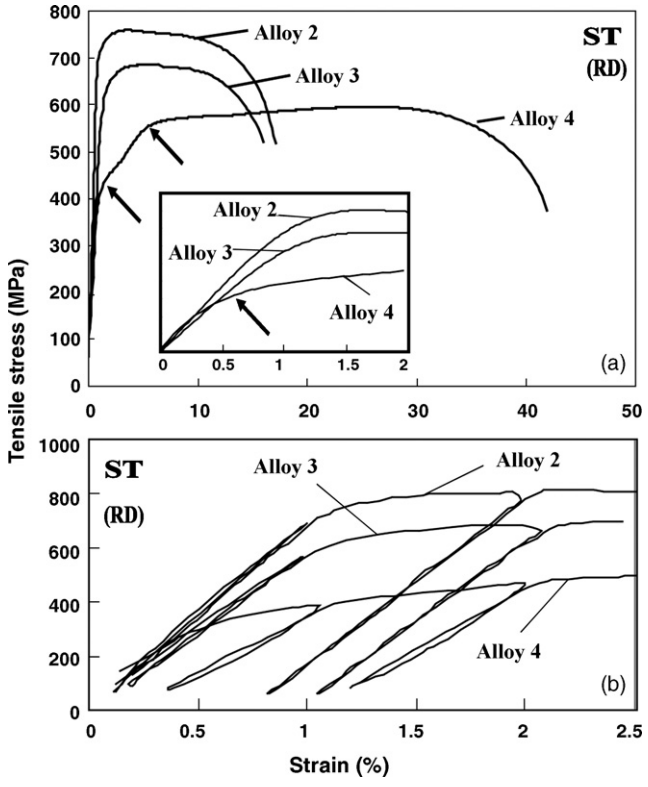

Fig. 10. Tensile stress–strain curves for alloys 2–4 in the rolling direction, RD, after solution treatment, and the inset in the elastic zone shown in an enlarged scale (a) and loading–unloading curves in the elastic zone (b).

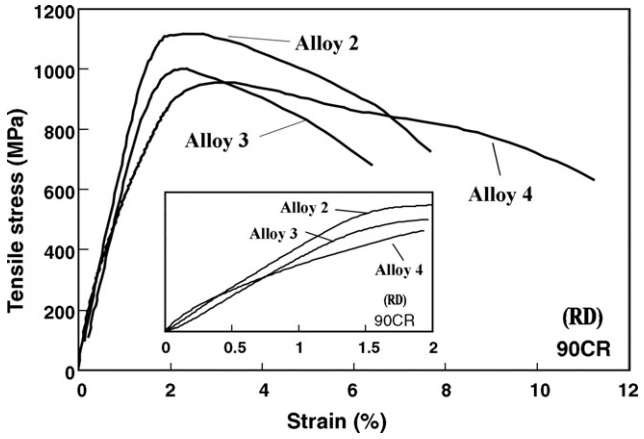

Fig. 11. Tensile stress–strain curve for alloys 2–4 in the rolling direction, RD, after 90% cold rolling. The inset in the elastic zone shown in an enlarged scale.

remaining due to the untransformed martensite during unloading, because a large activation energy is needed for the martensite to retransform to the β-phase. It is important to mention here that the alloy 4 in the 90CR condition exhibited very small pseudoelasticity and only one yielding point appeared as shown in Fig. 11.

The UTS and the ELS values with the testing directions are listed in Table 3. In the 90CR condition, both the UTS and the ELS were higher in RD than in 45° to RD due to the texture developed by cold rolling. The difference in the UTS and ELS between RD and 45° to RD seemed to increase with increasing β-phase stability. However, the alloy 3 in the ST condition exhibited the UTS and the ELS higher in 45° to RD than in RD owing to the presence of the recrystallization texture in it. So, as the β-phase stability increased, the anisotropy in the plastic properties increased in 90CR specimens, whereas decreased in ST specimens. This was attributable to the appearance of the permanent plastic rolling texture or the recrystallization texture in the alloys, depending on the β-phase stability as explained earlier.

3.6. Effect of β-phase stability on the work hardening rate

Here, the work hardening rate (WHR) is defined by the average increase in the stress for a 1% strain increment in the plastic strain range from 2.5% to the strain before necking starts. The WHR changed with the β-phase stability. For example, the WHR values for alloys 2, 3 and 4 in the ST condition were −0.15, 0.07 and 0.5 MPa, respectively. They changed form negative to positive values across the $\beta/\beta+\alpha''$ boundary as the β-phase stability decreased. However as shown in Fig. 11, any alloys in the 90CR condition never showed the work hardening after yielding, but instead necking occurred just after yielding.

The Vickers hardness of conventional β-titanium alloys is known to increase gradually by cold rolling due to the work hardening effect. As shown in Fig. 9, the four designed alloys were hardened by the first rolling and the increment in the hardness during the subsequent cold rolling seemed to decrease with decreasing β-phase stability. Also it may be due to the activation of secondary or even tertiary slipping systems by deformation as was observed in the alloy 3 (see Fig. 6). So, this least stable β-alloy will possess a minimum work hardening rate and it will behave like super plastic, while showing a high cold workability.

It is important in this aspect to mention that the small addition of oxygen into the least stable single β-phase alloy has been experienced to be effective in achieving no work hardening deformation, and there is no attendant increase in the hardness by cold working as is observed in Ti–20 mass% Mo [2] and GUM metals [6].

3.7. Change in elastic properties with β-phase stability

3.7.1. Young's modulus

Conventional alloys exhibit a linear relation between stress and strain in the elastic zone. However, as shown in Figs. 10 and 11 a non-linear relation was observed in the ST and 90% CR specimens. This result is similar to the result of GUM metals [6].

For the ST specimens, as shown in Fig. 12, the alloy 3 had the lower average Young's modulus than the alloy 2 in the rolling direction (RD), as indicated by dashed lines. The alloy 4 had highest initial value but the lowest average Young's modulus in most of the elastic zone among them due to the presence of the α″-phase in the β-phase matrix and also due to the pseudoelastic effect. In the 45° direction, however, the alloy 3 showed a higher initial value than the alloy 2 as indicated by solid lines, but the lower average Young's modulus than the alloy 2 in most of the elastic zone. So the present results confirm our previous study [7] that the Young's modulus decreases as the β-phase stability decreases.

As shown in Fig. 13, the 90CR specimens showed almost the same results as the ST specimens, except for a general increase in the Young's modulus by about 5, 10 and 20 GPa for alloys 2, 3 and 4, respectively. Beside these, for the single β-phase alloys 2 and 3, the attainable elastic strain was about 1.5% in the 90CR conditions as shown in Fig. 11, which was higher than the elastic strain, 1.1%, in the ST condition as shown in Fig. 10. This is because, the alloy with the $\{1\,0\,0\}\langle 1\,1\,0\rangle$ texture has a larger tensile elastic strain than that with the $\{2\,1\,1\}\langle 1\,1\,0\rangle$ texture [3]. Also as shown in Fig. 13, in case of the alloy 2, the Young's modulus in the most elastic zone was lower in the 45° direction than in the RD due to the presence of the strong $\{1\,0\,0\}\langle 1\,1\,0\rangle$

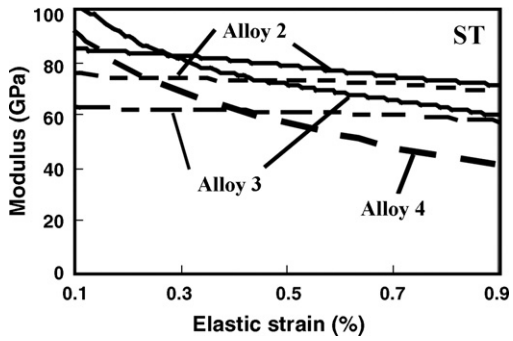

Fig. 12. Change in the average Young's modulus with elastic strain after ST in the RD of alloys 2, 3 and 4 (dashed line) and in the 45° inclined to RD of alloys 2 and 3 (solid line).

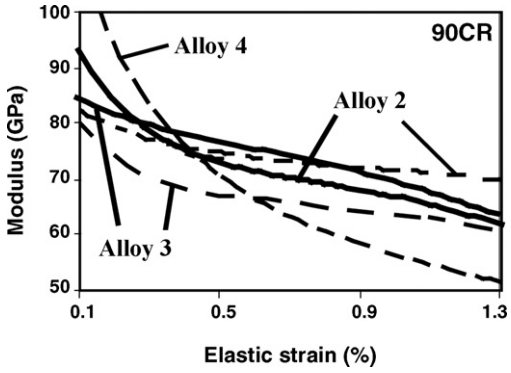

Fig. 13. Change in the average Young's modulus with elastic strain after 90% CR, 90CR, in the RD of alloys 2, 3 and 4 (dashed line) and in the 45° inclined to RD of alloys 2 and 3 (solid line).

rolling texture in it, as discussed elsewhere [3,12].

It is important to mention here that the CR alloys showed a higher non-linearity compared to the ST alloys since the non-linearity is related to the accumulated elastic strain stored in the alloy by the cold rolling [16], and by the onset of stress-induced martensite in the alloy 4. As a result, the non-linearity was more remarkable in the alloys with the lower β-phase stability. This result is consistent with a well-known fact that as the β-phase stability decreases, the elastic shear modulus, C', decreases and then the elastic anisotropy constant, A, increases [9,10].

As shown in Fig. 12, there was a clear anisotropy of elastic properties in the alloys 2 and 3 in the ST condition, since the average Young's modulus was smaller in the RD than in the 45° inclined to RD. Also, the elastic anisotropy was higher in the alloy 3 than in the alloy 2 which is the further confirmation of the above discussion on the effect of β-phase stability on both C' and A. However, this is not the case in the 90CR condition because of the two factors affecting in the opposite way; one is the strength of the developed texture and the other is the C' and A, see Fig. 13.

3.7.2. Resilience

The resilience is a measure of the potential for an alloy to absorb energy without plastic or permanent deformation, and it is calculated from the area under the stress–strain curve in the elastic zone. Here the upper stresses of the elastic deformation were chosen to be 850 and 600 MPa in the CR and ST conditions, respectively. As shown in Table 3, the resilience generally increased with decreasing β-phase stability in both the ST and the 90CR conditions. Also, the resilience seemed higher in 45° to RD than in RD.

4. Conclusion

The $\beta/\beta+\alpha''$ phases boundary was found to be located in the extended $\overline{Bo}$–$\overline{Md}$ diagram between the alloy 3 and the alloy 4. The tendency of forming the $\{1\,0\,0\}\langle 1\,1\,0\rangle$ texture by cold rolling increased as the β-phase becomes more stable, resulting in the larger anisotropy of the plastic properties in the higher β-phase stability alloys. On the contrary, the recrystallization texture was more enhanced in the lower β-phase stability alloys resulting in the larger anisotropy of the plastic properties. Also, the anisotropy of the elastic properties increased as the β-phase stability decreased in the ST condition, but there was no clear trend in the CR condition. The non-linearity in the elastic zone of the stress–strain curve was larger in the lower β-stability alloys. Also, the work hardening tended to decrease with lowering β-phase stability, and then the super plastic-like deformability was found to be higher in those alloys which were located closely to the $\beta/\beta+\alpha''$ boundary as reported in GUM metals.

Acknowledgments

The authors acknowledge the Computer Center, Institute for Molecular Science, Okazaki National Institute for the use of supercomputer. This research was supported by the Grant-in-Aid for Scientific Research from the Ministry of Education, Science, Sports and Culture of Japan, and from the Japan Society for the Promotion of Science. The authors are grateful to Prof. H. Ezaki in Suzuka College of Technology for his valuable support during tensile testing.

References

[1] S. Ishiyama, S. Hanada, O. Izumi, ISIJ Int. 31 (1991) 807–813.
[2] Y. Takemoto, I. Shimizu, A. Sakakibara, M. Hida, Y. Mantani, Mater. Trans. 45 (2004) 1571–1576.
[3] H.Y. Kim, T. Sasaki, H. Hosoda, S. Miyazaki, Acta Mater. 54 (2006) 423–433.
[4] H. Matsumoto, S. Watanabe, S. Hanada, J. Alloys Compd. 439 (2007) 146–155.
[5] W. Xu, K.B. Kim, J. Das, M. Calin, J. Eckert, Scripta Mater. 54 (2006) 1943–1948.
[6] T. Saito, T. Furuta, J.H. Hwang, S. Kuramoto, K. Nishino, et al., Science 300 (2003) 464–467.
[7] M. Abdel-Hady, K. Henoshita, M. Morinaga, Scripta Mater. 55 (2006) 477–480.
[8] Y.N. Wang, J.C. Huang, Mater. Chem. Phys. 81 (2003) 11–26.
[9] H. Ikehata, N. Nagasako, T. Furuta, A. Fukumoto, K. Miwa, T. Saito, Phys. Rev. B 70 (2004) 174113.
[10] E.S. Fisher, D. Dever, Acta Metall. 18 (1970) 265–269.
[11] T. Inamura, Y. Fukui, H. Hosoda, S. Miyazaki, Mater. Sci. Forum. 475–479 (2005) 2323–2328.
[12] H. Matsumoto, S. Watanabe, S. Hanada, Mater. Trans. 46 (2005) 1070–1078.
[13] H. Hosoda, Y. Kinoshita, Y. Fukui, T. Inamura, M. Miyazaki, Mater. Sci. Eng. A 438–440 (2006) 870–874.
[14] H.R. Wenk, P. Van Houtte, Rep. Prog. Phys. 67 (2004) 1368.
[15] T. Furuta, S. Kuramoto, J. Hwang, K. Nishino, T. Saito, Mater. Trans. 46 (2005) 3001–3007.
[16] S. Kuramoto, T. Furura, J.H. Hwand, K. Nishino, T. Saito, Metall. Mater. Trans. A 37 (2006) 657–662.
[17] S.F. Castro, J. Gallego, F.J.G. Landgraf, H.J. Kestenbach, Mater. Sci. Eng. A 427 (2006) 301–305.
[18] O. Engler, Scripta Mater. 44 (2001) 229–236.
[19] E.W. Collings, Applied Superconductivity, Metallurgy and Physics of Titanium Alloys, vol. 1, Plenum Press, New York, 1986, pp. 464–469.